Mechanical properties of neutron-irradiated single crystal tungsten W(100) studied by indentation and FEM modelling

Spilios Dellis[1], Xiazi Xiao[2], Dmitry Terentyev[3,*], Konstantina Mergia[1,*], Spyros Krimpalis[1], Spyros Messoloras[1] and Alexander Bakaev[3]

[1]NCSR Demokritos, Institute of Nuclear and Radiological Science and Technology, Energy and Safety, 15310 Agia Paraskevi, Greece

[2]Department of Mechanics, School of Civil Engineering, Central South University, Changsha 410075, P.R. China

[3]SCK•CEN, Nuclear Materials Science Institute, Boeretang 200, 2400 Mol, Belgium

Abstract

The aim of this work is to investigate the effect of high-temperature neutron irradiation on the mechanical properties of single-crystal tungsten W(100) studied by non-destructive mechanical testing and modelling. Neutron irradiation up to 0.12 displacements per atom was performed at 600, 800, 900 and 1200 °C in the Belgium material test reactor BR2 at SCK•CEN in Mol. The mechanical properties of the irradiated tungsten were assessed by impulse excitation and depth-sensing indentation measurements. The values of Young's modulus, shear modulus and Poisson ratio are not affected by the irradiation. The mean hardness of the irradiated tungsten increases by 48, 45, 46, and 34 % after irradiation at 600, 800, 900 and 1200 °C, respectively. The results obtained by the instrumented hardness tests were used as inputs for the finite element method model, applied to deduce the contributions coming from the neutron irradiation defects to the plastic deformation upon the indentation process, which include the impediment of sliding dislocations by sessile defects and modification of surface morphology due to the inhibited strain hardening ability through the dislocation-defect interaction. The validation of the fitted constitutive laws was realized by the crystal plasticity finite element method (CP-FEM) model, which was applied to simulate the indentation load-depth curves with certain assumptions on the irradiation-induced microstructure and calculate the distribution of stress under the indenter to investigate the extension of the plastic zone in the process of the indentation.

Keywords: tungsten, plasma facing materials, neutron irradiation, radiation damage, indentation, impulse excitation technique, crystal plasticity, finite element method

*Corresponding authors: K. Mergia, email: kmergia@ipta.demokritos.gr, D. Terentyev, email: dmitry.terentyev@sckcen.be

1 Introduction

Tungsten (W) is the candidate material for plasma-facing components (PFCs) in ITER and DEMO reactors due to its high melting temperature, high thermal conductivity, low tritium retention, good sputtering resistance, low swelling, thermal stress and shock resistance, and high-temperature strength [1,2]. Application of tungsten in a monoblock design concept does not imply structural function, however, the concern on the loss of vacuum accident requires structural integrity of the PFC component under operation [3]. It is well known that W suffers from a brittle fracture at low temperatures, with a ductile to brittle transition temperature (DBTT) ranging from room temperature to several hundred degrees Celsius [2], which causes a limitation of its application in the water-cooled PFCs. Several methods of microstructure modification [4,5,6,7] have been proposed to cope with the problem of tungsten's low toughness, among which, cold rolling and forging are the most promising ones. The actual operating temperature of tungsten will depend on the location of PFC and reactor design. The lower operation temperature boundary is defined by tungsten's DBTT while the upper limit should not exceed the recrystallization temperature, whose nominal onset is above 1300 ^{o}C in pure W (the recrystallization onset is expected to be significantly lower for a duration of operation of thousands of hours) [8,9].

In a fusion environment tungsten will be subjected to a high flux (up to $7 \cdot 10^{18}$ $m^{-2}s^{-1}$) of high energy neutrons (up to 14 MeV) accompanied by extreme heat fluxes (10-20 $MWm^{-2}s^{-1}$) and implantation of hydrogen (H) and helium (He) ash ejected from the plasma [10]. Neutron irradiation in tungsten generates three distinct types of structural damage. (a) Neutron reaction with W nuclei results to their transmutation to Rhenium (Re), Osmium (Os), and Tantalum (Ta) [11]. (b) Neutron collision cascades produce displacement damage in the form of Frenkel pairs, *i.e.* vacancies and interstitials, and their clusters, such as voids and dislocation loops [12,13]. (c) The induced damage facilitates radiation enhanced segregation and/or diffusion that results in the formation of W-Re-Os precipitates [14]. The population of each of these defects types dictates W's hardening/embrittlement and further increase its DBTT, that can go as high as 800 ^{o}C [15,16,17].

Irradiation conditions strongly influence the type of the defects that are produced in W. It is known that raising irradiation temperature and dose promotes voids formation and then precipitates, while dislocation loops prevail at temperatures below 500 °C [18]. In the literature, the formation of void lattice together with dislocation loops was observed after neutron irradiation of W at 550 °C [19]. Other studies of neutron irradiation of pure W at 500 °C revealed, apart from the formation of dislocation loops, the formation of sigma-phase (WRe) and chi-phase (WRe_3) precipitates containing

Re and Os, whereas at elevated temperatures (800 °C) only voids and precipitates are present [20]. With increasing damage level up to 1 dpa, the irradiation hardening of pure W begins to increase, and significant hardening occurs when highly dense precipitates (chi-phase) are formed [21]. Thus, the neutron irradiation has a drastic impact already at low irradiation doses, especially if the irradiation temperature is below 600 °C. Naturally, this will affect the material performance and will radically limit the service lifetime in terms of the structural integrity of the PFCs. Therefore, a combination of thermal cycling and accumulation of neutron irradiation damage in W may result in its cracking. This is one of the risks having the highest impact for water-cooled divertor concepts because in an accidental loss of vacuum, toxic and volatile tungsten trioxide particles will be formed. In the case of prolonged neutron irradiation, not only displacement damage but also the transmutation products of Re and Os will contribute to further degradation of thermal and mechanical properties due to irradiation induced diffusion resulting in precipitation [22,23,24]. Insight about the evolution of defects in neutron irradiated single crystal W and their effects in its mechanical properties is reported in a number of studies [21,25,26,27,28].

The aim of the current work is to investigate the effect of high temperature neutron irradiation on the mechanical properties of single crystal tungsten, W(100) and to establish a basic understanding of the underlying phenomena. Impulse excitation technique (IET) is employed to study the elastic properties of W(100), while depth sensing micro-indentation is used to measure the hardness, as well as their dependence on the irradiation temperature. The results obtained by the instrumented hardness tests are used as input for the finite element method model, applied to deduce the constitutive laws for the plastic deformation in the presence of the irradiation defects. The validation of the constitutive laws is realized by the crystal plasticity finite element method model, which was applied to simulate the indentation loading-depth curves. The physical mechanism behind the hardening of the irradiated W(100) is revealed employing the crystal plasticity finite element method (CP-FEM) by simulating the Vickers indentation loading curves and extracting the physical parameters describing the plastic deformation of the materials [29].

2 Experimental

2.1 Materials and irradiations

Single crystal W(100) rod of 99.99 % purity of 12 mm diameter was supplied from MaTeck. Circular disc shaped specimens of 1 mm thickness were sectioned using electrical discharge machining (EDM). The specimens were mechanically polished from both sides using SiC paper and diamond

suspension up to 0.25 μm, followed by polishing using 0.05 μm colloidal silica, achieving mirror-like surface and removing any surface oxide and stresses/surface damage induced by the EDM cutting. Prior to the indentation measurements, the samples were ultrasonically cleaned, and the quality of the samples' surface was evaluated employing optical microscopy. Preliminary experiments for evaluating the adequateness of the applied mechanical polishing process in the hardness measurements were also performed. Specifically, Vickers indentation experiments were performed on W(100) single crystal specimens that had been mechanically polished following the described procedure and on specimens in which the mechanical polishing was followed by an electropolishing step. It was found that the Vickers hardness and depth-load curves were the same within error bars showing that the applied polishing procedure was adequate for the indentation measurements and that the results are representative of the samples.

Neutron irradiation was performed in the Belgian Material Test Reactor (BR2). Fission reactors deliver mixed spectrum which causes transmutation rates of W into Re and Os to be higher compared to those expected in ITER and DEMO conditions. As a result, the accelerated production of Re/Os leads to radiation-induced precipitation as was discussed in refs. [21,28], where the irradiation-induced microstructure after HFIR and JOYO irradiation was compared. To minimize the transmutation, the irradiation was performed inside the fuel element in the maximum fast neutron (>0.1 MeV, $7 \cdot 10^{14}$ n/cm^2/s) flux position. The samples were encapsulated in a stainless steel tube, of 1.5 mm wall thickness, filled with helium. The thickness of the steel tube was adjusted to maximize the shielding from the thermal neutrons. The gap between the samples and the tube was adjusted to achieve 600, 800, 900 and 1200 $^{\circ}$C following the thermal and neutronic calculations. The irradiation dose was 0.12 displacement per atom (dpa), which was calculated by MCNPX 2.7.0 based on the total fast neutron fluence ($5.8 \cdot 10^{20}$ n/cm^2, >0.1 MeV) achieved after two irradiation cycles of a total duration of 49 days [30]. The dpa cross sections for W have been prepared from the JENDL4 file (MT444) for the threshold displacement energy of 55 eV, following the recommendation of International Atomic Energy Agency (IAEA) [31]. Furthermore, the value of 55 eV comes from a recent evaluation based on experimental measurements of single atomic displacements [32,33]. The transmutation of W into Re and Os is calculated based on the ALEPH code developed by SCK•CEN and available nuclear databases [34,35,36] and for the irradiation position and spectrum, the upper limit of the summed concentration (at%) of Re and Os is 0.35 %. The fraction of Os is about 1-5 % of the total produced Re and Os. The low concentration of Re and Os is in agreement with previously published results from transmission electron microscopy (TEM) investigation of neutron irradiated single crystal W.

2.2 Impulse excitation

The Young's modulus, *E*, the shear modulus, *G*, and the Poisson ratio, *v*, of the non-irradiated and irradiated W(100) samples were obtained employing IET [37] using the Buzz-o-Sonic system. For these tests, the disc shaped specimen was supported by a foam material and excited by a light mechanical impulse. The impulse tool used consisted of a steel ball (2 mm diameter) attached to the end of a thin elastic rod. A microphone located in the vicinity of the sample was used to transmit sound vibrations to the signal processing unit. The first and second natural resonant frequencies, $f_{1,2}$, are identified, which in turn can be used to calculate the values of $E_{1,2}$ corresponding to these frequencies using the following equation

$$E_{1,2} = \frac{12\pi d^2 f_{1,2}^2 m\left(1-v^2\right)}{K_{1,2}^2 t^3} \qquad \text{Eq. 1}$$

where *d*, *m*, and *t* are the diameter, mass and thickness of the sample, respectively. Using $d=2r$ and $m = V\rho = \pi r^2 t\rho$, where ρ, *r*, and *V* are the density, the radius and the volume of the specimen, respectively, Eq. 1 becomes

$$E_{1,2} = \frac{3\pi r^4 f_{1,2}^2 \rho\left(1-v^2\right)}{K_{1,2}^2 t^2} \qquad \text{Eq. 2}$$

v is determined according to ASTM E1876 [38] as a function of $2t/D$ and f_1/f_2. $K_{1,2}$ are the first and second natural geometric factors listed in ASTM E1876 as a function of *v* and $2t/D$. *G* is determined using the equation

$$G = \frac{E}{2\left(1-v^2\right)} \qquad \text{Eq. 3}$$

2.3 Indentation

Indentation experiments were performed employing NANOVEA's mechanical tester. During an indentation experiment an indenter of specified geometry, in our case a Vickers indenter, penetrates the surface of the material under investigation with constant loading rate. When the load reaches its set maximum value the indenter is held at this maximum load for a time period (holding time), and then the unloading takes place at the same rate with the loading. The load and penetration depth are measured versus time and these measurements are combined to give a load versus depth curve. In

this work, the maximum load was set at 3 N, while the (un)loading rate was 20 N/min. A holding time of 200 s was applied in all experiments before starting of the unloading process. The loading rate was selected after a series of indentation tests to achieve stability in the hardness values. The holding time was chosen such as to attain equilibrium conditions, *i.e.* almost no change of the indentation depth. A set of nine indentation tests, spaced by 200 μm, were performed. An optical microscope was used to select the indented area free from visible defects.

The hardness, H, of the samples was calculated using the projected area, A_p, of the residual imprint after the indentation tests determined from its optical microscopy images and the maximum applied force F_{max} through

$$H = \frac{F_{\max}}{A_p} = \frac{2F_{\max}}{d_{mean}^2}, \qquad \text{Eq. 4}$$

where d_{mean} is the mean diameter of the residual imprint.

3 Modelling

3.1 Single crystal plasticity theory

According to the classical crystal plasticity theory, deformation of materials consists of the elastic and plastic stages [39]. The plastic deformation is dominated by the dislocation motion in the slip system and this dislocation glide can be related to the viscoplastic strain rate, $\dot{\varepsilon}^{vp}$, by

$$\dot{\varepsilon}^{vp} = \sum_{a=1}^{N_s} \boldsymbol{R}^a \dot{\gamma}^a, \qquad \text{Eq. 5}$$

where N_s and $\boldsymbol{R}^{\alpha}$ are the number of slip systems and the Schmid factor, respectively. $\boldsymbol{R}^a = \frac{1}{2}\left(\boldsymbol{s}^a \otimes \boldsymbol{n}^a + \boldsymbol{n}^a \otimes \boldsymbol{s}^a\right)$, where the unit vectors for the slipping and normal direction of the α^{th} slip system are represented with $\boldsymbol{s}^{\alpha}$ and $\boldsymbol{n}^{\alpha}$, respectively. The plastic shear rate, $\dot{\gamma}^a$, for the α^{th} slip system can be described by

$$\dot{\gamma}^a = \dot{\gamma}_0 \left| \frac{\tau_{RSS}^a}{\tau_{CRSS}^a} \right|^{\frac{1}{m}} \operatorname{sgn}\left(\tau_{RSS}^a\right), \qquad \text{Eq. 6}$$

where $\dot{\gamma}_0$ and m are the reference shearing rate and strain rate sensitivity, respectively. τ^a_{RSS} is the resolved shear stress, and τ^a_{CRSS} is the critical resolved shear stress (CRSS). τ^a_{CRSS} is expressed by three hardening mechanisms as follows

$$\tau^{\alpha}_{CRSS} = \tau_{LF} + \tau^{\alpha}_{SSD} + \tau^{\alpha}_{DL}, \quad \text{Eq. 7}$$

where τ_{LF} is the lattice friction stress, τ^a_{SSD} is the dislocation hardening term, and τ^a_{DL} the hardening term from irradiation induced defects (DL).

For temperatures below 580 K, the τ_{LF} for W can be expressed as [29,40]

$$\tau_{LF} = \tau_{p0}\left[1-\sqrt{\frac{k_B T}{2H_k}\ln\left(\frac{\dot{\gamma}_{p0}}{\dot{\varepsilon}}\right)}\right], \quad \text{Eq. 8}$$

where τ_{p0} is the reference stress for the screw dislocation, k_B is the Boltzmann constant, $2H_k$ is the formation enthalpy of the kink pair on the screw dislocation and $\dot{\gamma}_{p0}$ is the reference strain rate. $\dot{\varepsilon}$ is the loading strain rate defined as in ref. [29].

The stress due to the dislocation hardening, τ^a_{SSD}, can be expressed as

$$\tau^a_{SSD} = Gbh_{SSD}\sqrt{\rho^a_{SSD}}, \quad \text{Eq. 9}$$

where h_{SSD} is the dislocation strength coefficient, b is the magnitude of Burgers vector and ρ^a_{SSD} the density of statistically stored dislocations (SSDs). As the plastic deformation progresses, the generation of SSDs within the plasticity affected region would result in the evolution of τ^a_{SSD}, *i.e.*

$$\dot{\tau}^a_{SSD} = \sum_{\beta=1}^{N_S} h^{\alpha\beta}_{SSD}\left|\dot{\gamma}^{\beta}\right|, \quad \text{Eq. 10}$$

where the hardening matrix for SSDs, $h^{\alpha\beta}_{SSD}$, is expressed as [41]

$$h^{\alpha\beta}_{SSD} = a_0\left|1-\frac{\tau^{\beta}_{SSD}}{\tau^{\max}_{SSD}}\right|^{n_0} m^{\alpha\beta}, \quad \text{Eq. 11}$$

In Eq. 11 α_0 and n_0 are the dislocation hardening coefficient and the dislocation interaction sensitivity coefficient, respectively. $m^{\alpha\beta}$ is the matrix describing the interaction strength between

dislocations gliding in slip systems α and β [42]. $\tau_{SSD}^{\max}$ denotes the maximum SSD hardening strength when the density of SSDs gets saturated.

Finally, stress due to the radiation induced defects hardening, τ_{DL}^{a}, can be expressed as

$$\tau_{DL}^{\alpha} = Gbh_{DL}\sqrt{N_{DL}d_{DL}} = Gbh_{DL}\sqrt{L_{DL}}\,, \qquad \text{Eq. 12}$$

where h_{DL} is the defect strength coefficient, N_{DL} is the number density of the induced defects and d_{DL} their mean diameter. h_{DL} is the strength of the obstacle (*i.e.* irradiation induced defects), which ranges from 0 (corresponding to no resistance) up to 1 (Orowan type of the interaction [43]), respectively. The obstacle strength for dislocation loops and voids was studied by atomistic simulations in bcc Iron (Fe) and it was found that h_{DL} varies between 0.2 to 0.8 depending on the loop size and orientation, and being 0.5 on average [44,45,46]. Given that no study was performed for W, we take h_{DL} to be 0.5 following the knowledge obtained for Fe, which should be relevant accounting that both W and Fe have the same crystallographic structure. The effective length of defects generated by irradiation, *i.e.*

$$L_{DL} = \frac{\int N_{DL}(\mathbf{r})\, d_{DL}(\mathbf{r})\, d^3\mathbf{r}}{V}, \qquad \text{Eq. 13}$$

has the physical meaning of the radiation induced obstacle length per unit volume. If we assume a mean diameter of defects or use that obtained by TEM, then their number density can be calculated based on the best fit of the FEM model to the experimental data.

The rate of the radiation hardening term is given by

$$\dot{\tau}_{DL}^{a} = \sum_{\beta=1}^{N_s} h_{DL}^{\alpha\beta}\left|\dot{\gamma}^{\beta}\right|, \qquad \text{Eq. 14}$$

where

$$h_{DL}^{\alpha\beta} = -\beta_0\left|\frac{\tau_{DL}^{\beta} - \tau_{DL}^{\min}}{\tau_{DL}^{\max} - \tau_{DL}^{\min}}\right|^{n_1} n^{\alpha\beta}, \qquad \text{Eq. 15}$$

is the defect hardening matrix, and β_0 is the defect hardening coefficient. $\tau_{DL}^{\max}$ and $\tau_{DL}^{\min}$ are, respectively, the maximum and minimum defect hardening strength when the defect density reaches the maximum and minimum value. Further, the minimum value of irradiation induced defects density, N_{DL}, is taken as one-tenth of the maximum value of N_{DL}, *i.e.* the initial density of *DLs* before

indentation starts. n_1 is the defect interaction sensitivity coefficient. $n^{\alpha\beta}$ is the interaction matrix for the interaction between dislocation of the α^{th} slip plane and *DLs* on the β^{th} habit plane. Specifically, $\left[n^{\alpha\beta}\right] = P_0$ when the normal direction of the α^{th} slip plane is not parallel to the normal direction of the β^{th} habit plane of *DLs*, otherwise, $\left[n^{\alpha\beta}\right] = 0$. The assumption on the minimum value of N_{DL} is purely empirical and based on our earlier study made for the neutron irradiated Fe-Cr alloys [47,48].

The annihilation of irradiation-induced defects by plastic deformation is considered in the constitutive equations (*via* Eq. 15). The details behind the formulae to account for the removal of the irradiation defects can be found in our earlier works [47,48].

3.2 Finite element method model setup

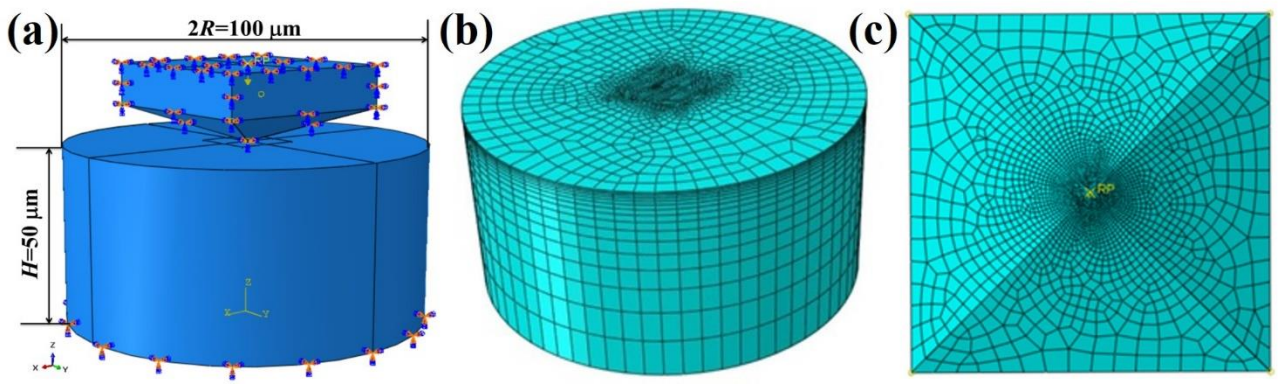

Figure 1. (a) Schematic of the geometrical model for the indentation of tungsten with a Vickers indenter. The indentation is represented as a cylinder with a height of 50 μm and a radius of 50 μm. (b) The meshes of the sample and the Vickers indenter with the tip radius of 100 nm employed in these experiments

The theoretical model developed in the previous subsection is applied to simulate the indentation of W(100) with the Vickers indenter. The constitutive equations are implemented into the subroutine VUMAT of Abaqus. For the simulations, the sample is to be a cylinder with a height of 50 μm and a radius of 50 μm as illustrated in Figure 1(a). The meshed elements for the sample and Vickers indenter are shown in Figure 1(b) and (c), respectively. The sample consists of 31212 linear hexahedral elements of type C3D8R and 33696 nodes, and the Vickers indenter is taken as a rigid body meshed with R3D4 and R3D3 elements. For the region beneath the indenter tip, the mesh is refined with the minimum size of 0.1 μm and 0.25 μm along the z-axis direction and in the x-y plane, respectively. The bottom of the sample is fixed, and the rest surfaces are free of constraints. The

interaction between the sample surface and the indenter tip is set as frictionless as it has a little effect on the force-depth relationship [49].

In the simulations, the constant force increment boundary condition is applied. As the maximum loading force is 3 N and the loading rate 20 N/min, the loading time is set to 9 s. Thus the loading strain rate can be estimated as $\dot{\varepsilon} = \frac{\frac{\Delta L}{t}}{H} \approx \frac{\frac{4.5\ \mu m}{9\ s}}{50\ \mu m} = 0.01\ s^{-1}$. By substituting this strain rate into Eq. 8, the obtained lattice friction, τ_{LF} , is 409 MPa.

Table I. Parameters of the constitutive law for tungsten.

Parameter	Value	Units	Used in	Ref.
$\dot{\gamma}_0$	0.001	s^{-1}	Eq. 6	[50]
m	0.05		Eq. 6	
h_{SSD}	0.26		Eq. 9	
τ_{p0}	1038	MPa	Eq. 8	[40]
H_k	$1.65 \cdot 10^{-19}$	J	Eq. 8	
$\dot{\gamma}_{p0}$	$3.71 \cdot 10^{10}$	s^{-1}	Eq. 8	
G	159	GPa	Eq. 9	Current study
ρ^1_{SSD}	$1 \cdot 10^{10}$	m^{-2}	Eq. 9	According to TEM initially it is below 10^{11} m^{-2}, while after tensile plastic deformation at RT it reaches 10^{15} m^{-2}
$\rho^1_{SSD,saturated}$	$1 \cdot 10^{15}$	m^{-2}	Eq. 9	
α_0	165	MPa	Eq. 11	Fitted (unirradiated)
n_0	4.0		Eq. 11	
h_{DL}	0.5		Eq.12	See text
$N^{\min}_{DL}$	$0.1\, N^{\max}_{DL}$		Eq. (12) & (15)	
β_0	$5 \cdot 10^8$	Pa	Eq. 15	Common Fitted for irradiated samples
n_1	2		Eq. 15	
$[n^{\alpha\beta}]=P_0$	1		Eq. 15	
$N_{DL} \cdot d_{DL}$			Eq. 12	Fitted

4 Results and Discussion

4.1 Elastic properties

The Young's modulus, *E*, and shear modulus, *G*, and Poisson ratio, *v*, of the non-irradiated and irradiated W(100) single crystal were determined as described in Section 2.2 and are presented in Table II. The values for the unirradiated sample are in a good agreement with literature data [51,52,53]. The elastic properties of the irradiated sample remain the same, within error bars, with those before the irradiation. It can thus be concluded that neutron irradiation to a dose of 0.12 dpa for irradiation temperatures in the range 600 to 1200 ^{o}C does not affect the elastic properties of W(100).

Table II. Experimentally determined Young's modulus, *E*, shear modulus, *G*, Poisson's ratio, *v*, hardness, $\langle H \rangle$ and H_0 (Eq. 16) of unirradiated and irradiated W(100) single crystal to 0.12 dpa. Also, from the model fitting the effective length of defects, L_{DL}, the defect number density, N_{DL}, and the volume fraction, *f*, of the defects assuming spherical size with a diameter of 5 nm.

T_{irr} (^{o}C)	*E* (GPa)	*G* (GPa)	*v*	$\langle H \rangle$ (GPa)	H_0 (GPa)	L_{DL} (10^{15} m·m^{-3})	N_{DL} (10^{23} m^{-3})	*f* (%)
Unirradiated	400 ± 7	160 ± 3	0.28 ± 0.03	3.68 ± 0.03	0.016 ± 0.003	-	-	
600	410 ± 6	161 ± 3	0.27 ± 0.03	5.43 ± 0.03	0.487 ± 0.003	4.0	8.0	5.24
800	402 ± 6	158 ± 3	0.27 ± 0.03	5.32 ± 0.03	0.34 ± 0.01	1.75	3.5	2.29
900	407 ± 6	160 ± 2	0.27 ± 0.03	5.36 ± 0.05	0.257 ± 0.006	2.0	4.0	2.62
1200	405 ± 6	159 ± 3	0.28 ± 0.03	4.92 ± 0.04	0.094 ± 0.007	1.25	2.5	1.63

4.2 Vickers Hardness

From the optically determined diameter of the Vickers' indenter imprint and Eq. 4, the hardness of the material was determined. The hardness of single crystal materials can vary, depending on the azimuthal indenter orientation with respect to the in-plane crystallographic axes [54]. Vickers indentation experiments with different indenter azimuthal angle were performed in the unirradiated and irradiated W(100) single crystal specimens.

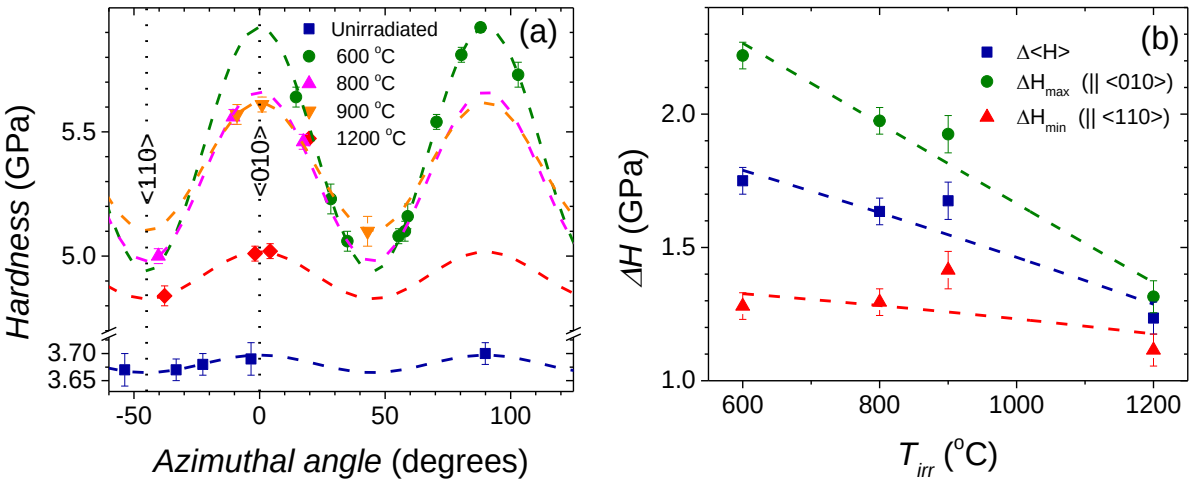

Figure 2. (a) Hardness versus azimuthal angle of unirradiated and irradiated W(100) single crystal. The dashed lines are least square fits to the data as described in the text. The vertical dotted lines show the two in-plane crystallographic orientations. (b) Hardness increase versus irradiation temperature for the mean hardness and that at 0 and 45 degrees azimuthal angles. The dashed lines are least square fits to the data as a guide to the eye.

The obtained hardness as a function of the azimuthal angle, ϕ, of the diagonals of the indenter with respect to the in-plane crystallographic directions is presented in Figure 2a. The experimental data can be fitted using the equation

$$H = \langle H \rangle + H_0 \sin\left(2\pi \frac{\phi + 22.5}{90}\right), \qquad \text{Eq. 16}$$

where $\langle H \rangle$ is the mean hardness over all azimuthal angles and H_0 is the amplitude of the sinusoidal modulation. When the diagonal of the indenter is along the <010> direction ϕ is zero resulting to the highest hardness value, while when the diagonal of the indenter is along the <110> direction ϕ is 45° resulting to the lowest hardness value.

The mean hardness, $\langle H \rangle$, of the unirradiated W(100) material was found 3.68±0.05 GPa. We observe that $\langle H \rangle$ after irradiation at 600 °C increases by a factor of approximately 1.5 compared to the unirradiated sample (Table II). Irradiation at higher temperature results to a smaller increase relatively to the unirradiated sample (Table II). The increase of the hardness with irradiation is related to the formation of dislocation loops and vacancy clusters or voids. No precipitates from the transmutation products are expected to form at this low irradiation dose. Similar hardness values

after irradiation in the temperature range 609-830 °C for a similar dose have been reported by *Garrison et al* [25].

A variation in the amplitude, H_0, that depends on the irradiation temperature is also observed (Table II). In the unirradiated sample a very small variation, with peak to peak around 0.03 GPa, in the hardness with respect to the azimuthal angle is observed, while after irradiation at 600 ^{o}C it increases to about 1 GPa. Increase in the irradiation temperature results to smaller hardness variation with respect to the azimuthal angle, with the specimen irradiated at 1200 ^{o}C exhibiting a hardness variation of about 0.19 GPa.

The irradiation induced hardening, $\Delta H = H(irradiated) - H(unirradiated)$, in presented in Figure 2(b) for the mean value of the hardening $\Delta\langle H\rangle = \langle H(irradiated)\rangle - \langle H(unirradiated)\rangle$ and at 0 and 45 degrees angle, $\Delta H_{\max}\left(\phi = 0^{o}\right) = \Delta H_{\max}\left(\| \langle 010\rangle\right)$, and $\Delta H_{\min}\left(\phi = 45^{o}\right) = \Delta H_{\min}\left(\| \langle 110\rangle\right)$, respectively.

In Figure 3(b) the load-depth curves (mean value of nine tests) obtained from the depth-sensing Vickers indentation experiments, with an azimuthal angle of 0 degrees, which is also the azimuthal angle of the indenter with respect to the crystallographic direction of the W sample in the CP-FEM simulation, on unirradiated and irradiated at 600 ^{o}C single crystal W(100) specimens are presented. These curves show that after the irradiation the same maximum load is achieved at a swallower penetration depth compared to the non-irradiated sample, thereby indicating a hardening effect due to the neutron irradiation induced defects.

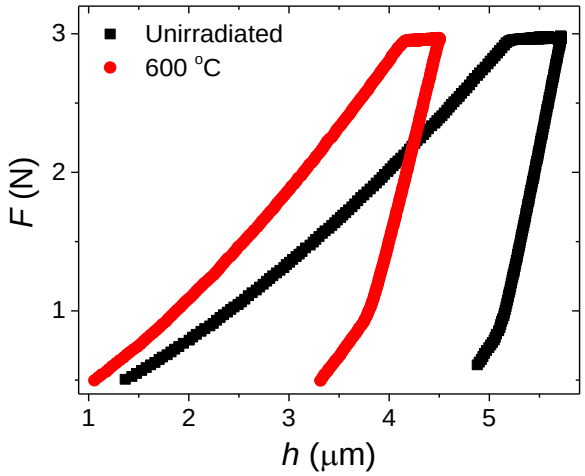

Figure 3. Load-depth curves of unirradiated and irradiated at 600 ^{o}C W(100) single crystal.

Figure 4 shows the images of the residual impression after the Vickers indentation tests on unirradiated and irradiated samples to 0.12 dpa at 600 and 1200 °C for two azimuthal angles (indenter diagonals approximately parallel to $\langle 010 \rangle$ and $\langle 110 \rangle$ directions). On the contrary to the unirradiated specimen, after irradiation at 600 °C W(100) presents an intense localized pile-up formation exhibiting a four-fold symmetry, which is more apparent when the indenter diagonals are at 45 degrees with the crystallographic axes, (Figure 4(b) and (e)) for both azimuthal angles. Black arrows in Figure 4(b) and (e) indicate slip steps that reveal slip localization and slip channel formation. This phenomenon has been observed in several previous studies on a variety of irradiated metals [55,56,57,58]. The proposed physical mechanism describing this behaviour is based on the hypothesis that the irradiation induced defect clusters are annihilated/moved by gliding dislocations creating defect free channels that facilitate the movement of subsequent dislocations [59,60,61,62,63]. This behaviour is observed at a lower degree after irradiation at higher temperatures (Figure 4(c) and (f)).

It should be noted that when the indenter diagonals are at an angle different than zero with the crystallographic axes the imprint shapes are not regular but deformed and their exact shapes are dependent on the orientation of the indented surface. The plastic flow patterns induced at the contact boundary are along the preferential slip directions located at the subsurface region.

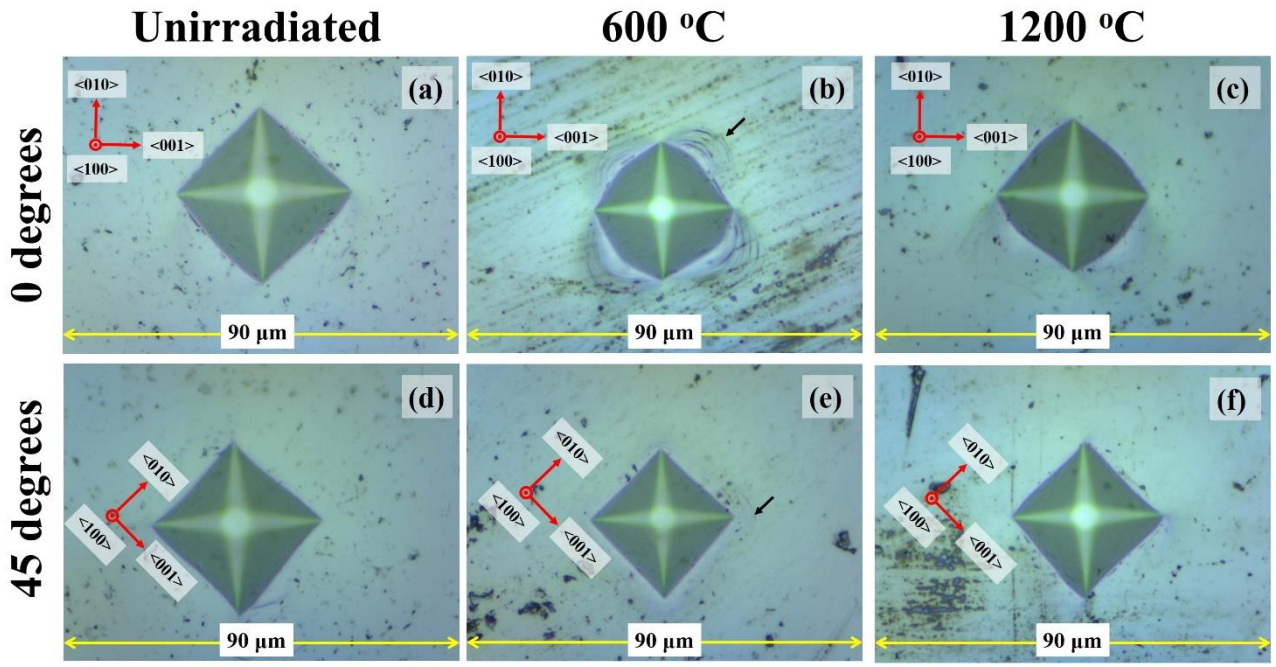

Figure 4. Images of residual imprints after Vickers indentation tests on (a, d) unirradiated and irradiated at (b, e) 600 °C and (c, f) 1200 °C W(100) single crystal.

4.3 CP-FEM simulation

4.3.1 Unirradiated Single Crystal W(100)

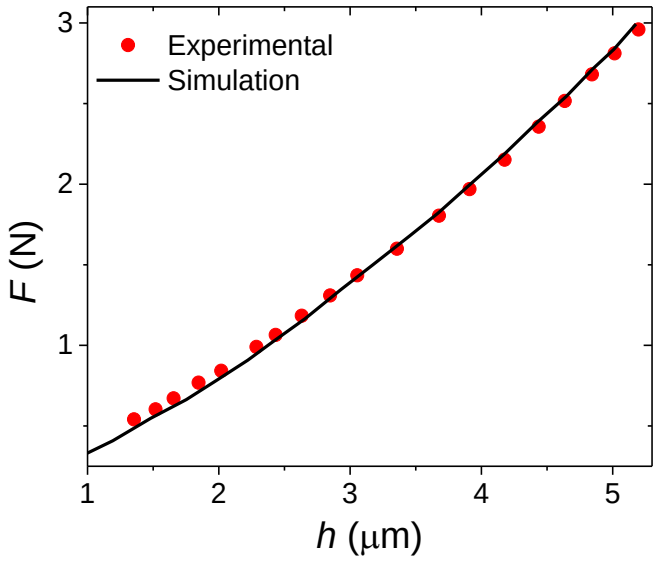

Figure 5. Experimental (red dot) and simulated (black line) of the loading part of the depth-load curve of Vickers indentation experiment on unirradiated W(100).

For the fitting of the loading part of the depth-load curve the parameters of Table I were incorporated. From the fitting of the data of the unirradiated W(100) sample (Figure 5), the values of the dislocation hardening coefficient, α_0, and the dislocation interaction sensitivity coefficient, n_0, of Eq. 11 were found to be 165 MPa, and 4.0, respectively. It is noted that the strain gradient was not considered in the CP-FEM simulations. This was based on the fact that the indentation size effects induced by strain gradient are not manifested when indentation depth exceeds beyond 0.5 μm, where the bulk hardness of the material can be reliably measured [29,64]. This leads to the deviation of the simulated data from the experimental ones for shallow depth penetrations as it is observed in Figure 5 and Figure 7.

In Figure 6(a) and 6(b), the images of the experimental and simulated residual imprints of the non-irradiated W(100) sample are presented. The simulated imprint (Figure 6(b)) indicates that the surface topography produced by the indentation load exhibits an upward (pile-up) deformation around the imprint with respect to the original surface plane. The distribution of the dislocation hardening term, τ_{SSD}^{1}, resulting from the distribution of the ρ_{SSD}^{1}, after the indentation test, is presented in Figure 6(c).

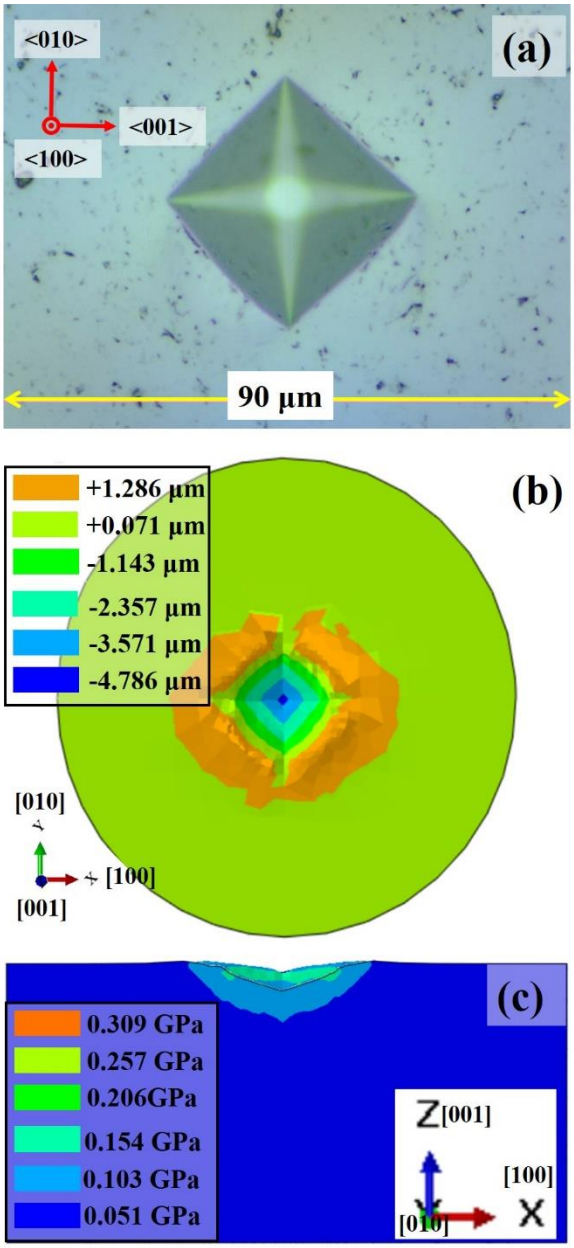

Figure 6. Experimental (a) and simulated (b) residual imprints of unirradiated W(100). (c) Distribution of the dislocation hardening term, τ_{SSD}^{1}, for the slip system (110)[1-11] for maximum indentation applied load of 3 N applied along [100].

4.3.2 Irradiated Single Crystal W(100)

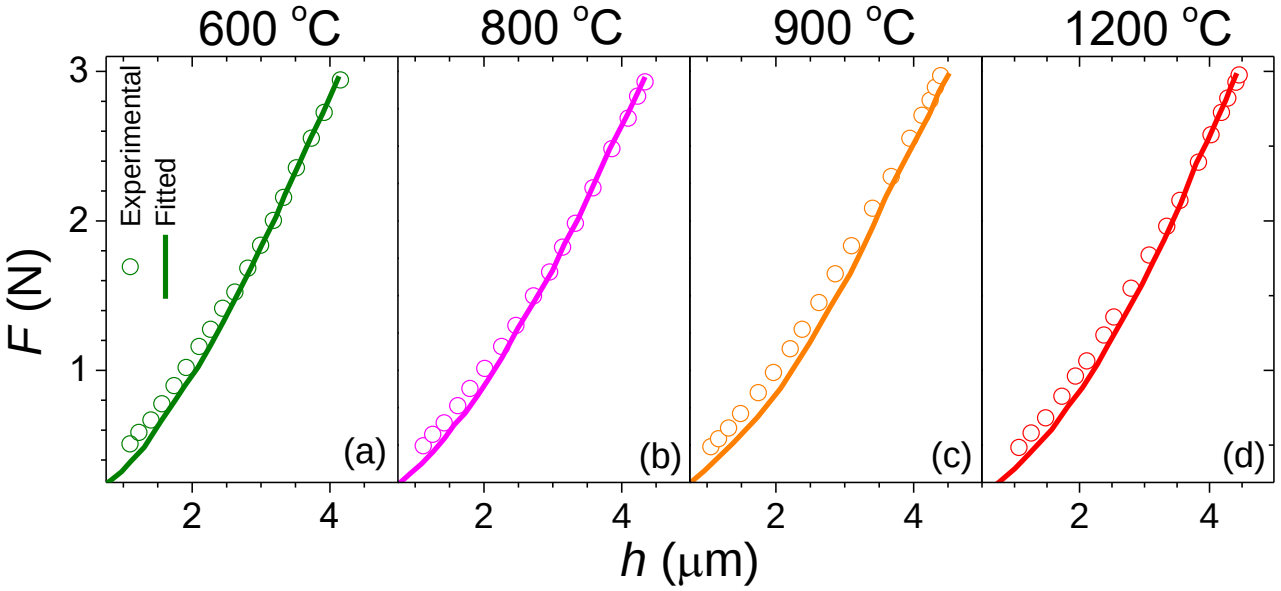

Figure 7. Experimental (circles) and simulated (line) depth-load curve of the loading part of Vickers indentation experiment on irradiated W(100) to 0.12 dpa at (a) 600, (b) 800, (c) 900, and (d) 1200 °C.

Initially, the values of the dislocation hardening coefficient, α_0, and the dislocation interaction sensitivity coefficient, n_0, were determined from the fitting to the unirradiated sample data (Table I) and these were used for the fitting of the depth-load curves (Figure 7) for the irradiated samples. From the fitting of the depth-load curves (Figure 7) of the irradiated samples the effective length of obstacles, L_{DL}, was determined (see Eq. 13). The values of L_{DL} are presented in Table II and its variation as a function of the irradiation temperature is presented in Figure 8(a). It is observed that as the irradiation temperature increases the effectiveness of irradiation in producing obstacles to the moving dislocations is reduced. If the type of defects and their size remains the same at the different irradiation temperatures it could be said that their number is reduced as the irradiation temperature increases. This reduction with temperature can be explained by assuming a diffusion controlled self-annealing process acting to the generated defects. As the self-annealing mechanism is diffusion controlled it is apparent that the annihilation of defects will be higher the higher the irradiation temperature is. Therefore, there will be an irradiation temperature, T_c, at which all the irradiation generated defects will be self-annealed. This temperature will be close to the melting point. Under the above physics reasoning, the data of Figure 8(a) have been fitted to the empirical equation

$$L_{LD} = L_0 e^{-c\frac{T_{irr}}{T_c - T_{irr}}}, \qquad \text{Eq. 17}$$

where L_0=(10.1±4.7)·10^{15} m/m^3, c =4.7±1.7, T_c was taken the melting point of tungsten, *i.e.* 3422 °C and T_{irr} in °C. The large errors are due to the limited number of points.

It is expected that the effective length of obstacles produced by the irradiation and the measured hardness values will be correlated. This is verified in Figure 8(b) where the correlation between L_{DL} and $\Delta\langle H\rangle$ can be described by the equation

$$\Delta\langle H\rangle = \Delta H_{\infty}\left(1-e^{-\frac{L_{DL}}{L_0}}\right), \qquad \text{Eq. 18}$$

where ΔH_{∞}=1.8±0.1 GPa and L_0=(0.9±0.2)·10^{-5} m/m^3.

Further, it was assumed that the defect strength coefficient, h_{DL}, is 0.5 and the diameter of the defects, d_{DL}, is around 5 nm. The assumption for d_{DL} is based on preliminary results of a TEM study (the complete study is to be published). This assumption is also supported by the results of previously published TEM studies of neutron irradiated W single crystals. These studies showed that W single crystal irradiated at conditions close to those in the current work exhibit voids and dislocation loops having a mean size close to 5 nm [25,26,27,28]. Thus, from the fitted values of $L_{DL} = N_{DL}\cdot d_{DL}$, the number density of the irradiation induced defects, N_{DL}, was determined (Table II). The obtained values of N_{DL} are close to the up to now reported values in the literature for defects density in neutron irradiated single crystal tungsten (between 10^{22} and 10^{23} m^{-3}) [18,26,28,65]. The increase of the number density or the volume fraction of the irradiation induced defects is lower the higher the irradiation temperature.

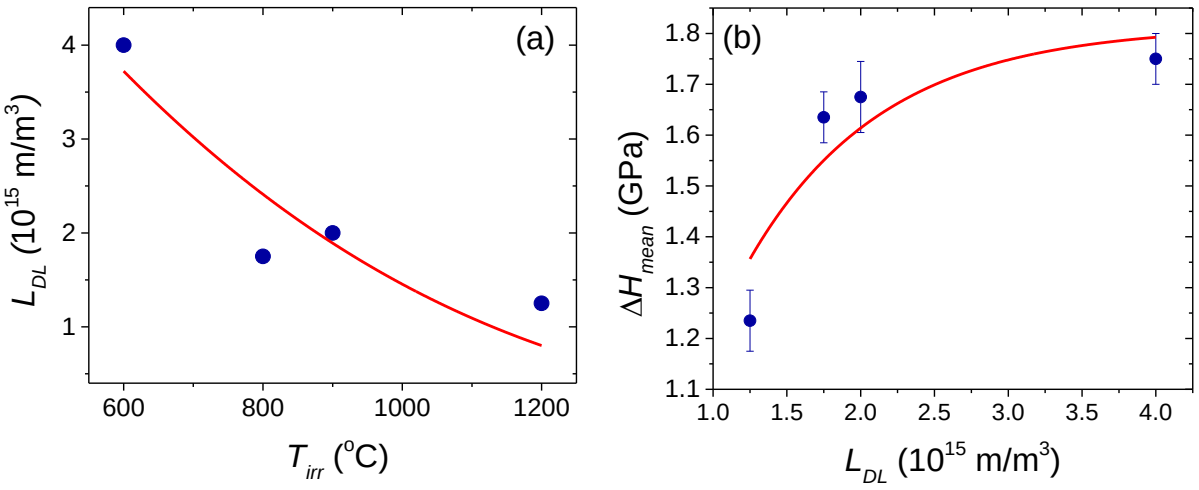

Figure 8. (a) The effective defect length versus irradiation temperature. The solid line is a least square fit to the data (see text). (b) Mean hardness increase versus the effective defect length. The solid line is a least square fit to the data (see text).

The residual and the simulated imprints left on the irradiated W(100) specimens for all the investigated irradiation temperatures are presented in Figure 9(a-d) and (e-h), respectively. Surface topography of the simulated imprints of the unirradiated and irradiated samples shows pile-ups (Figure 6b and Figure 9(e-h)). However, the pile-up's pattern of the irradiated samples is extended to a smaller area compared to the unirradiated one. The reduction of the area around the imprint that exhibits pile-ups, after irradiation, is also illustrated in the distribution of τ^1_{SSD} in the z-direction (Figure 9(i-l)), in which it is observed that τ^1_{SSD} reaches the bulk value closer to the surface in the irradiated samples compared to the unirradiated one (Figure 6(c)). The morphology of the residual imprints is in qualitative agreement with that of the simulated ones although this is not so apparent for the unirradiated sample (Figure 6). For the unirradiated sample there is a variation between the simulated and experimental imprints which is attributed to the difference of the screw and edge dislocation mobility. At room temperature, edge dislocations move freely in the unirradiated material while screw dislocations are practically immobile [66]. In the irradiated tungsten the movement of all dislocations (screw, edge and mixed) is inhibited by irradiation defects and this results in the formation of pile-up. This could be the reason that the CP-FEM model fails to accurately predict the surface topography of the unirradiated sample since it is based on the activation and slip of screw dislocations.

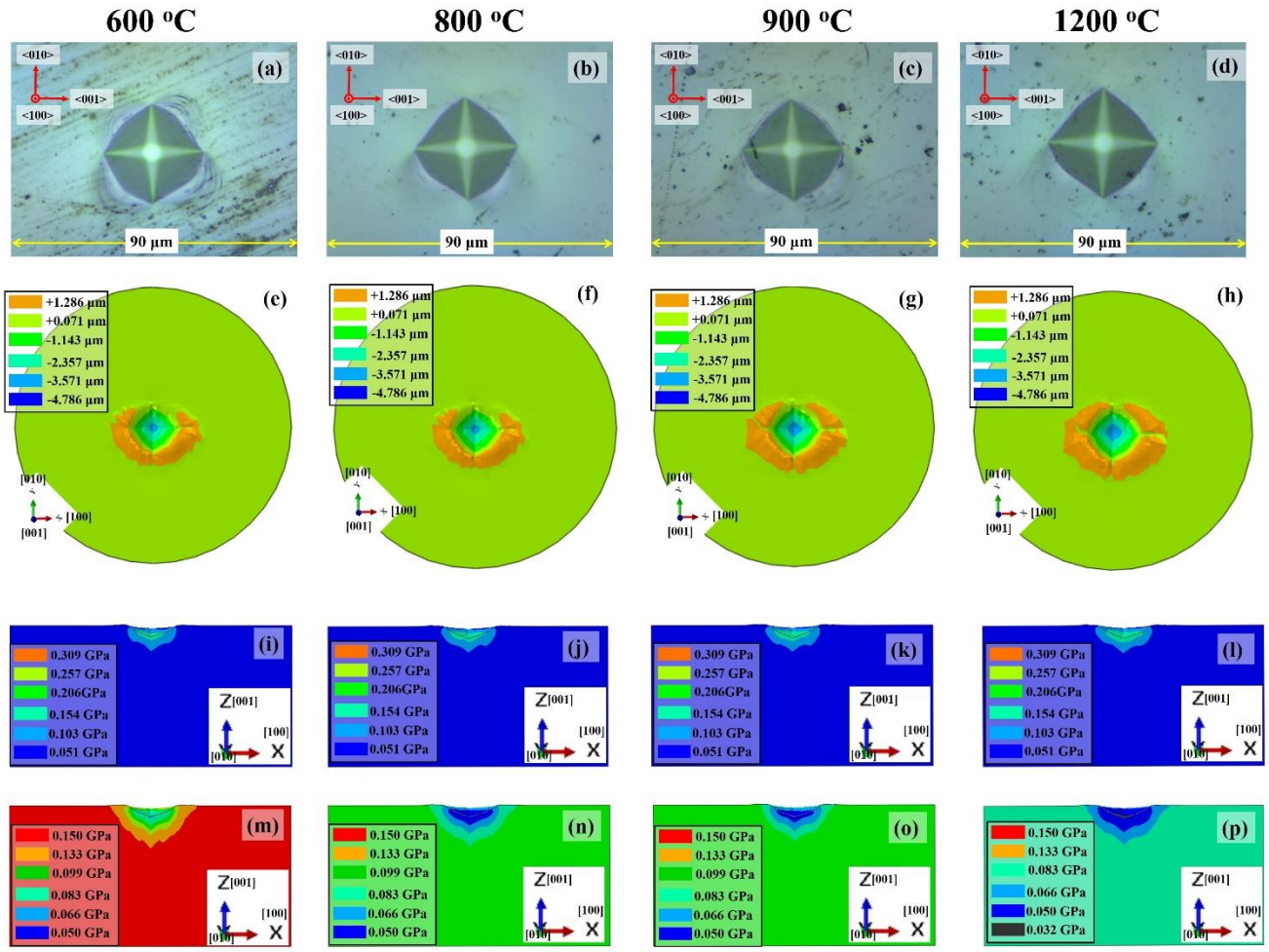

Figure 9. Experimental (a-d) residual imprints of Vickers indenter and simulated (e-h) ones for the irradiated W(100) in the temperature range 600-1200 °C. The calculated stress distribution, τ_{SSD}^{1}, due to dislocation hardening (i-l) and the stress distribution, τ_{DL}^{1}, due to the irradiation induced defects (m-p), for the slip system (110)[1-11] for maximum applied load of 3 N applied along [100].

5 Summary and Conclusions

Mechanical properties of W(100) single crystal irradiated with fission neutrons at 0.12 dpa in the temperature range 600-1200 °C were investigated by Vickers indentation and Impulse Excitation techniques. The force-depth curves of the indentation experiment have been simulated by Finite Element Analysis and the use of the crystal plasticity model (CP-FEM). Good agreement between the experimentally determined load-depth curves and those calculated by CP-FEM is observed. The experimental and residual imprints of the irradiated samples are in good qualitative agreement. The modelling by CP-FEM is further validated by the very good correlation between the calculated

irradiation induced defect density and the measured hardness at the different irradiation temperatures.

The neutron irradiation does not influence the elastic properties of the material as revealed by the IET measurements. It may be concluded that the nature and extent of the irradiation induced defect do not change measurably the average atomic forces of the crystal. On the other hand, the hardness of the W(100) increases in all the irradiation temperatures. This indicates that the generated radiation defects have a large influence on the dislocation movement and the plastic behaviour of the crystal. Irradiation at 600 °C increases the hardness by 48 %, while the CP-FEM simulations show an irradiation induced defect density of about $8 \cdot 10^{23}$ m^{-3}. Irradiation at higher temperatures results in a lower increase of the induced defect number density. The decrease of the number of the generated defects with the irradiation temperature might be related to the annealing/migration of the defects during the irradiation. Specifically, during the irradiation of W(100) at high temperature, two competitive processes take place, the creation of defects in the material and the annealing of these defects. *Hu et al.* presented the results of isochronal annealing of irradiated single crystal W to 0.006 and 0.03 dpa at a temperature of 90 ºC [65]. According to this work, the annealing up to 800 ºC results in the increase of the number density of vacancy-type defects while a further increase of the annealing temperature causes its decrease, explained as recombination with available dislocation loops/lines and coalescence of vacancy defects into larger voids. Thus, the trend obtained here for the N_{DL} reflects this behaviour, *i.e.* the low irradiation temperature promotes the creation of a higher number of defects compared to the irradiation above 600 ºC, given the same neutron fluence. This self-healing mechanism is important for the application of W in a fusion environment at high temperatures.

Acknowledgements

This work has been carried out within the framework of the EUROfusion Consortium and has received funding from the Euratom research and training programme 2014-2018 and 2019-2020 under Grant Agreements No. 633053. The views and opinions expressed herein do not necessarily reflect those of the European Commission.

---

[1] S. Wurster, N. Baluc, M. Battabyal, T. Crosby, J. Du, C. García-Rosales, A. Hasegawa, A. Hoffmann, A. Kimura, H. Kurishita, R.J. Kurtz, H. Li, S. Noh, J. Reiser, J. Riesch, M. Rieth, W. Setyawan, M. Walter, J.H. You, R. Pippan, Recent progress in R&D on tungsten alloys for divertor structural and plasma facing materials, J. Nucl. Mater. 442 (2013) 181–189. doi:10.1016/j.jnucmat.2013.02.074.

[2] G. Pintsuk, Tungsten as a plasma-facing material, Elsevier Inc., 2012. doi:10.1016/B978-0-08-056033-5.00118-X.

[3] D. Stork, P. Agostini, J.L. Boutard, D. Buckthorpe, E. Diegele, S.L. Dudarev, C. English, G. Federici, M.R. Gilbert, S. Gonzalez, A. Ibarra, C. Linsmeier, A. Li Puma, G. Marbach, P.F. Morris, L.W. Packer, B. Raj, M. Rieth, M.Q. Tran, D.J. Ward, S.J. Zinkle, Developing structural, high-heat flux and plasma facing materials for a near-term DEMO fusion power plant: The EU assessment, J. Nucl. Mater. 455 (2014) 277–291. doi:10.1016/j.jnucmat.2014.06.014.

[4] J. Riesch, J.Y. Buffiere, T. Höschen, M. Di Michiel, M. Scheel, C. Linsmeier, J.H. You, In situ synchrotron tomography estimation of toughening effect by semi-ductile fibre reinforcement in a tungsten-fibre-reinforced tungsten composite system, Acta Mater. 61 (2013) 7060–7071. doi:10.1016/j.actamat.2013.07.035.

[5] Q. Wei, H.T. Zhang, B.E. Schuster, K.T. Ramesh, R.Z. Valiev, L.J. Kecskes, R.J. Dowding, L. Magness, K. Cho, Microstructure and mechanical properties of super-strong nanocrystalline tungsten processed by high-pressure torsion, Acta Mater. 54 (2006) 4079–4089. doi:10.1016/j.actamat.2006.05.005.

[6] H. Kurishita, S. Matsuo, H. Arakawa, S. Kobayashi, K. Nakai, T. Takida, K. Takebe, M. Kawai, Superplastic deformation in W-0.5 wt.% TiC with approximately 0.1 μm grain size, Mater. Sci. Eng. A. 477 (2008) 162–167. doi:10.1016/j.msea.2007.05.009.

[7] M. Rieth, J. Reiser, B. Dafferner, S. Baumgärtner, The impact of refractory material properties on the helium cooled divertor design, Fusion Sci. Technol. 61 (2012) 381–384. doi:10.13182/FST12-1T3.

[8] H. Bolt, V. Barabash, W. Krauss, J. Linke, R. Neu, S. Suzuki, N. Yoshida, Materials for the plasma-facing components of fusion reactors, J. Nucl. Mater. 329–333 (2004) 66–73. doi:10.1016/j.jnucmat.2004.04.005.

[9] K. Tsuchida, T. Miyazawa, A. Hasegawa, S. Nogami, M. Fukuda, Recrystallization behavior of hot-rolled pure tungsten and its alloy plates during high-temperature annealing, Nucl. Mater. Energy. 15 (2018) 158–163. doi:10.1016/j.nme.2018.04.004.

[10] M. Rieth, S.L. Dudarev, S.M. Gonzalez De Vicente, J. Aktaa, T. Ahlgren, S. Antusch, D.E.J. Armstrong, M. Balden, N. Baluc, M.F. Barthe, W.W. Basuki, M. Battabyal, C.S. Becquart, D. Blagoeva, H. Boldyryeva, J. Brinkmann, M. Celino, L. Ciupinski, J.B. Correia, A. De Backer, C. Domain, E. Gaganidze, C. García-Rosales, J. Gibson, M.R. Gilbert, S. Giusepponi, B. Gludovatz, H. Greuner, K. Heinola, T. Höschen, A. Hoffmann, N. Holstein, F. Koch, W. Krauss, H. Li, S. Lindig, J. Linke, C. Linsmeier, P. López-Ruiz, H. Maier, J. Matejicek, T.P. Mishra, M. Muhammed, A. Muñoz, M. Muzyk, K. Nordlund, D. Nguyen-Manh, J. Opschoor, N. Ordás, T. Palacios, G. Pintsuk, R. Pippan, J. Reiser, J. Riesch, S.G. Roberts, L. Romaner, M. Rosiński, M. Sanchez, W. Schulmeyer, H. Traxler, A. Ureña, J.G. Van Der Laan, L. Veleva, S. Wahlberg, M. Walter, T. Weber, T. Weitkamp, S. Wurster, M.A. Yar, J.H. You, A. Zivelonghi, Recent progress in research on tungsten materials for nuclear fusion applications in Europe, J. Nucl. Mater. 432 (2013) 482–500. doi:10.1016/j.jnucmat.2012.08.018.

[11] M.R. Gilbert, J.C. Sublet, Neutron-induced transmutation effects in W and W-alloys in a fusion environment, Nucl. Fusion. 51 (2011). doi:10.1088/0029-5515/51/4/043005.

[12] T. Troev, N. Nankov, T. Yoshiie, Simulation of displacement cascades in tungsten irradiated by fusion neutrons, Nucl. Instruments Methods Phys. Res. Sect. B Beam Interact. with Mater. Atoms. 269 (2011) 566–571. doi:10.1016/j.nimb.2011.01.010.

[13] R.C. Rau, R.L. Ladd, J. Moteff, Voids in irradiated tungsten and molybdenum, J. Nucl. Mater. 33 (1969) 324–327. doi:10.1016/0022-3115(69)90029-4.

[14] M.J. Lloyd, R.G. Abernethy, M.R. Gilbert, I. Griffiths, P.A.J. Bagot, D. Nguyen-Manh, M.P. Moody, D.E.J. Armstrong, Decoration of voids with rhenium and osmium transmutation products in neutron irradiated single crystal tungsten, Scr. Mater. 173 (2019) 96–100. doi:10.1016/j.scriptamat.2019.07.036.

[15] R.G. Abernethy, J.S.K.L. Gibson, A. Giannattasio, J.D. Murphy, O. Wouters, S. Bradnam, L.W. Packer, M.R. Gilbert, M. Klimenkov, M. Rieth, H.C. Schneider, C.D. Hardie, S.G. Roberts, D.E.J. Armstrong, Effects of neutron irradiation on the brittle to ductile transition in single crystal tungsten, J. Nucl. Mater. 527 (2019) 151799. doi:10.1016/j.jnucmat.2019.151799.

[16] I. V. Gorynin, V.A. Ignatov, V. V. Rybin, S.A. Fabritsiev, V.A. Kazakov, V.P. Chakin, V.A. Tsykanov, V.R. Barabash, Y.G. Prokofyev, Effects of neutron irradiation on properties of refractory metals, J. Nucl. Mater. 191–194 (1992) 421–425. doi:10.1016/S0022-3115(09)80079-2.

[17] J.M. Steichen, Tensile properties of neutron irradiated TZM and tungsten, J. Nucl. Mater. 60 (1976) 13–19. doi:10.1016/0022-3115(76)90112-4.

[18]A. Hasegawa, M. Fukuda, S. Nogami, K. Yabuuchi, Neutron irradiation effects on tungsten materials, Fusion Eng. Des. 89 (2014) 1568–1572. doi:10.1016/j.fusengdes.2014.04.035.

[19] V.K. Sikka, J. Moteff, Superlattice of voids in neutron‐irradiated tungsten, J. Appl. Phys. 43 (1972) 4942–4944. doi:10.1063/1.1661050.

[20] M. Fukuda, K. Yabuuchi, S. Nogami, A. Hasegawa, T. Tanaka, Microstructural development of tungsten and tungsten-rhenium alloys due to neutron irradiation in HFIR, J. Nucl. Mater. 455 (2014) 460–463. doi:10.1016/j.jnucmat.2014.08.002.

[21] A. Hasegawa, M. Fukuda, K. Yabuuchi, S. Nogami, Neutron irradiation effects on the microstructural development of tungsten and tungsten alloys, J. Nucl. Mater. 471 (2016) 175–183. doi:10.1016/j.jnucmat.2015.10.047.

[22] R.G. Abernethy, Predicting the performance of tungsten in a fusion environment: a literature review, Mater. Sci. Technol. 33 (2017) 388–399. doi:10.1080/02670836.2016.1185260.

[23] Y. Katoh, L.L. Snead, L.M. Garrison, X. Hu, T. Koyanagi, C.M. Parish, P.D. Edmondson, M. Fukuda, T. Hwang, T. Tanaka, A. Hasegawa, Response of unalloyed tungsten to mixed spectrum neutrons, J. Nucl. Mater. 520 (2019) 193–207. doi:10.1016/j.jnucmat.2019.03.045.

[24] M. Fujitsuka, B. Tsuchiya, I. Mutoh, T. Tanabe, T. Shikama, Effect of neutron irradiation on thermal diffusivity of tungsten-rhenium alloys, J. Nucl. Mater. 283–287 (2000) 1148–1151. doi:10.1016/S0022-3115(00)00170-7.

[25] L.M. Garrison, Y. Katoh, N.A.P.K. Kumar, Mechanical properties of single-crystal tungsten irradiated in a mixed spectrum fission reactor, J. Nucl. Mater. 518 (2019) 208–225. doi:10.1016/j.jnucmat.2019.02.050.

[26] X. Hu, T. Koyanagi, M. Fukuda, N.A.P.K. Kumar, L.L. Snead, B.D. Wirth, Y. Katoh, Irradiation hardening of pure tungsten exposed to neutron irradiation, J. Nucl. Mater. 480 (2016) 235–243. doi:10.1016/j.jnucmat.2016.08.024.

[27] M. Fukuda, N.A.P. Kiran Kumar, T. Koyanagi, L.M. Garrison, L.L. Snead, Y. Katoh, A. Hasegawa, Neutron energy spectrum influence on irradiation hardening and microstructural development of tungsten, J. Nucl. Mater. 479 (2016) 249–254. doi:10.1016/j.jnucmat.2016.06.051.

[28] T. Koyanagi, N.A.P.K. Kumar, T. Hwang, L.M. Garrison, X. Hu, L.L. Snead, Y. Katoh, Microstructural evolution of pure tungsten neutron irradiated with a mixed energy spectrum, J. Nucl. Mater. 490 (2017) 66–74. doi:10.1016/j.jnucmat.2017.04.010.

[29] X. Xiao, D. Terentyev, A. Ruiz, A. Zinovev, A. Bakaev, E.E. Zhurkin, High temperature nano-indentation of tungsten: Modelling and experimental validation, Mater. Sci. Eng. A. 743 (2019) 106–113. doi:10.1016/j.msea.2018.11.079.

[30] D.B. Pelowitz, J.W. Durkee, J.S. Elson, M.L. Fensin, J.S. Hendricks, M.R. James, R.C. Johns, G.W. Mckinney, S.G. Mashnik, J.M. Verbeke, L.S. Waters, T.A. Wilcox, MCNPX 2.7.0 Extensions, 2011. http://mcnpx.lanl.gov (accessed June 10, 2020).

[31] S.L. Dudarev, DPA definition and estimates, 2015. https://www-amdis.iaea.org/CRP/IrradiatedTungsten/RCM2/RCM2Presentation-DudarevDPA-2015-09-10.pdf.

[32] D.R. Mason, X. Yi, M.A. Kirk, S.L. Dudarev, Elastic trapping of dislocation loops in cascades in ion-irradiated tungsten foils, J. Phys. Condens. Matter. 26 (2014). doi:10.1088/0953-8984/26/37/375701.

[33] F. Maury, M. Biget, P. Vajda, Frenkel pair creation and stage I recovery in W crystals irradiated near threshold, Radiat. Eff. 38 (1978) 53–65. doi:10.1080/00337577808233209.

[34] A. Stankovskiy, G. Van Den Eynde, Advanced method for calculations of core burn-up, activation of structural materials, and spallation products accumulation in accelerator-driven systems, Sci. Technol. Nucl. Install. 2012 (2012). doi:10.1155/2012/545103.

[35] D.A. Brown, M.B. Chadwick, R. Capote, A.C. Kahler, A. Trkov, M.W. Herman, A.A. Sonzogni, Y. Danon, A.D. Carlson, M. Dunn, D.L. Smith, G.M. Hale, G. Arbanas, R. Arcilla, C.R. Bates, B. Beck, B. Becker, F. Brown, R.J. Casperson, J. Conlin, D.E. Cullen, M.A. Descalle, R. Firestone, T. Gaines, K.H. Guber, A.I. Hawari, J. Holmes, T.D. Johnson, T. Kawano, B.C. Kiedrowski, A.J. Koning, S. Kopecky, L. Leal, J.P. Lestone, C. Lubitz, J.I. Márquez Damián, C.M. Mattoon, E.A. McCutchan, S. Mughabghab, P. Navratil, D. Neudecker, G.P.A. Nobre, G. Noguere, M. Paris, M.T. Pigni, A.J. Plompen, B. Pritychenko, V.G. Pronyaev, D. Roubtsov, D. Rochman, P. Romano, P. Schillebeeckx, S. Simakov, M. Sin, I. Sirakov, B. Sleaford, V. Sobes, E.S. Soukhovitskii, I. Stetcu, P. Talou, I. Thompson, S. van der Marck, L. Welser-Sherrill, D. Wiarda, M. White, J.L. Wormald, R.Q. Wright, M. Zerkle, G. Žerovnik, Y. Zhu, ENDF/B-VIII.0: The 8th Major Release of the Nuclear Reaction Data Library with CIELO-project Cross Sections, New Standards and Thermal Scattering Data, Nucl. Data Sheets. 148 (2018) 1–142. doi:10.1016/j.nds.2018.02.001.

[36] A.Y. Konobeyev, U. Fischer, Y.A. Korovin, S.P. Simakov, Evaluation of effective threshold displacement energies and other data required for the calculation of advanced atomic displacement cross-sections, Nucl. Energy Technol. 3 (2017) 169–175. doi:10.1016/j.nucet.2017.08.007.

[37] G. Martinček, The determination of poisson's ratio and the dynamic modulus of elasticity from the frequencies of natural vibration in thick circular plates, J. Sound Vib. 2 (1965) 116–127. doi:10.1016/0022-460X(65)90089-1.

[38] ASTM Standard E1876–01, Standard Test Method for Dynamic Young's Modulus, Shear Modulus, and Poisson's Ratio by Impulse Excitation of Vibration, ASTM Int. (2005) 16. doi:10.1520/E1876-09.responsibility.

[39] R. Hill, J.R. Rice, Constitutive analysis of elastic-plastic crystals at arbitrary strain, J. Mech. Phys. Solids. 20 (1972) 401–413. doi:10.1016/0022-5096(72)90017-8.

[40] H. Lim, C.C. Battaile, J.D. Carroll, B.L. Boyce, C.R. Weinberger, A physically based model of temperature and strain rate dependent yield in BCC metals: Implementation into crystal plasticity, J. Mech. Phys. Solids. 74 (2015) 80–96. doi:10.1016/j.jmps.2014.10.003.

[41] A. Staroselsky, L. Anand, Inelastic deformation of polycrystalline face centered cubic materials by slip and twinning, J. Mech. Phys. Solids. 46 (1998) 671–696. doi:10.1016/S0022-5096(97)00071-9.

[42] A. Arsenlis, D.M. Parks, Modeling the evolution of crystallographic dislocation density in crystal plasticity, J. Mech. Phys. Solids. 50 (2002) 1979–2009. doi:10.1016/S0022-5096(01)00134-X.

[43] G.S. Was, Fundamentals of radiation materials science: Metals and alloys, second edition, 2016. doi:10.1007/978-1-4939-3438-6.

[44] D. Terentyev, D.J. Bacon, Y.N. Osetsky, Reactions between a 1/2 ⟨111⟩ screw dislocation and ⟨100⟩ interstitial dislocation loops in alpha-iron modelled at atomic scale, Philos. Mag. 90 (2010) 1019–1033. doi:10.1080/14786430903019073.

[45] D. Terentyev, Y.N. Osetsky, D.J. Bacon, Competing processes in reactions between an edge dislocation and dislocation loops in a body-centred cubic metal, Scr. Mater. 62 (2010) 697–700. doi:10.1016/j.scriptamat.2010.01.034.

[46] Y.N. Osetsky, D.J. Bacon, Comparison of void strengthening in fcc and bcc metals: Large-scale atomic-level modelling, Mater. Sci. Eng. A. 400–401 (2005) 374–377. doi:10.1016/j.msea.2005.02.083.

[47] X. Xiao, D. Terentyev, L. Yu, A. Bakaev, Z. Jin, H. Duan, Investigation of the thermo-mechanical behavior of neutron-irradiated Fe-Cr alloys by self-consistent plasticity theory, J. Nucl. Mater. 477 (2016) 123–133. doi:10.1016/j.jnucmat.2016.05.012.

[48] X. Xiao, D. Terentyev, L. Yu, D. Song, A. Bakaev, H. Duan, Modelling irradiation-induced softening in BCC iron by crystal plasticity approach, J. Nucl. Mater. 466 (2015) 312–315. doi:10.1016/j.jnucmat.2015.08.017.

[49] Y. Wang, D. Raabe, C. Klüber, F. Roters, Orientation dependence of nanoindentation pile-up patterns and of nanoindentation microtextures in copper single crystals, Acta Mater. 52 (2004) 2229–2238. doi:10.1016/j.actamat.2004.01.016.

[50] D. Terentyev, X. Xiao, A. Dubinko, A. Bakaeva, H. Duan, Dislocation-mediated strain hardening in tungsten: Thermo-mechanical plasticity theory and experimental validation, J. Mech. Phys. Solids. 85 (2015) 1–15. doi:10.1016/j.jmps.2015.08.015.

[51] R. Lowrie, A.M. Gonas, Single-Crystal Elastic Properties of Tungsten from 24° to 1800°C, J. Appl. Phys. 38 (1967) 4505–4509. doi:10.1063/1.1709158.

[52] D.I. Bolef, J. De Klerk, Elastic Constants of Single-Crystal Mo and W between 77° and 500°K, J. Appl. Phys. 33 (1962) 2311–2314. doi:10.1063/1.1728952.

[53] F.H. Featherston, J.R. Neighbours, Elastic constants of tantalum, tungsten, and molybdenum, Phys. Rev. 130 (1963) 1324–1333. doi:10.1103/PhysRev.130.1324.

[54] P. Filippov, U. Koch, Nanoindentation of aluminum single crystals: Experimental study on influencing factors, Materials (Basel). 12 (2019) 1–16. doi:10.3390/ma12223688.

[55] S. Das, H. Yu, E. Tarleton, F. Hofmann, Hardening and Strain Localisation in Helium-Ion-Implanted Tungsten, Sci. Rep. 9 (2019) 18354. doi:10.1038/s41598-019-54753-3.

[56] T.S. Byun, N. Hashimoto, K. Farrell, Deformation mode map of irradiated 316 stainless steel in true stress-dose space, J. Nucl. Mater. 351 (2006) 303–315. doi:10.1016/j.jnucmat.2006.02.033.

[57] N. Hashimoto, T.S. Byun, K. Farrell, S.J. Zinkle, Deformation microstructure of neutron-irradiated pure polycrystalline vanadium, J. Nucl. Mater. 336 (2005) 225–232. doi:10.1016/j.jnucmat.2004.09.017.

[58] K. Farrell, T.S. Byun, N. Hashimoto, Deformation mode maps for tensile deformation of neutron-irradiated structural alloys, J. Nucl. Mater. 335 (2004) 471–486. doi:10.1016/j.jnucmat.2004.08.006.

[59] M.J. Makin, J. V. Sharp, A Model of "Lattice" Hardening in Irradiated Copper Crystals with the External Characteristics of "Source" Hardening, Phys. Status Solidi. 9 (1965) 109–118. doi:10.1002/pssb.19650090114.

[60] T. Byun, N. Hashimoto, Strain Localization in Irradiated Materials, Nucl. Eng. Technol. 38 (2006) 619–638.

[61] H. Neuhäuser, R. Rodloff, Determination of the Velocity and Local Density of Mobile Dislocations Within Slip Bands in Neutron-Irradiated Copper by High Speed Cinematography, Phys. Status Solidi. 24 (1974) 549–555. doi:10.1002/pssa.2210240222.

[62] M.J. Makin, S.A. Manthorpe, The annealing of neutron irradiation hardening in copper crystals, Philos. Mag. 10 (1964) 579–594. doi:10.1080/14786436408228480.

[63] S.J. Zinkle, B.N. Singh, Microstructure of neutron-irradiated iron before and after tensile deformation, J. Nucl. Mater. 351 (2006) 269–284. doi:10.1016/j.jnucmat.2006.02.031.

[64] W.Z. Yao, J.H. You, Berkovich nanoindentation study of monocrystalline tungsten: a crystal plasticity study of surface pile-up deformation, Philos. Mag. 97 (2017) 1418–1435. doi:10.1080/14786435.2017.1299237.

[65] X. Hu, T. Koyanagi, M. Fukuda, Y. Katoh, L.L. Snead, B.D. Wirth, Defect evolution in single crystalline tungsten following low temperature and low dose neutron irradiation, J. Nucl. Mater. 470 (2016) 278–289. doi:10.1016/j.jnucmat.2015.12.040.

[66] X. Liu, S.I. Golubov, C.H. Woo, H. Huang, Glide of edge dislocations in tungsten and molybdenum, Mater. Sci. Eng. A. 365 (2004) 96–100. doi:10.1016/j.msea.2003.09.012.